NASA/TM—2015-218861

A Numerical Study on the Effect of Facesheet-Core Disbonds on the Buckling Load of Curved Honeycomb Sandwich Panels

Evan J. Pineda, David E. Myers, Brett A. Bednarcyk, and Thomas M. Krivanek
Glenn Research Center, Cleveland, Ohio

August 2015

NASA STI Program . . . in Profile

Since its founding, NASA has been dedicated to the advancement of aeronautics and space science. The NASA Scientific and Technical Information (STI) Program plays a key part in helping NASA maintain this important role.

The NASA STI Program operates under the auspices of the Agency Chief Information Officer. It collects, organizes, provides for archiving, and disseminates NASA's STI. The NASA STI Program provides access to the NASA Technical Report Server—Registered (NTRS Reg) and NASA Technical Report Server—Public (NTRS) thus providing one of the largest collections of aeronautical and space science STI in the world. Results are published in both non-NASA channels and by NASA in the NASA STI Report Series, which includes the following report types:

- TECHNICAL PUBLICATION. Reports of completed research or a major significant phase of research that present the results of NASA programs and include extensive data or theoretical analysis. Includes compilations of significant scientific and technical data and information deemed to be of continuing reference value. NASA counter-part of peer-reviewed formal professional papers, but has less stringent limitations on manuscript length and extent of graphic presentations.

- TECHNICAL MEMORANDUM. Scientific and technical findings that are preliminary or of specialized interest, e.g., "quick-release" reports, working papers, and bibliographies that contain minimal annotation. Does not contain extensive analysis.

- CONTRACTOR REPORT. Scientific and technical findings by NASA-sponsored contractors and grantees.

- CONFERENCE PUBLICATION. Collected papers from scientific and technical conferences, symposia, seminars, or other meetings sponsored or co-sponsored by NASA.

- SPECIAL PUBLICATION. Scientific, technical, or historical information from NASA programs, projects, and missions, often concerned with subjects having substantial public interest.

- TECHNICAL TRANSLATION. English-language translations of foreign scientific and technical material pertinent to NASA's mission.

For more information about the NASA STI program, see the following:

- Access the NASA STI program home page at http://www.sti.nasa.gov

- E-mail your question to help@sti.nasa.gov

- Fax your question to the NASA STI Information Desk at 757-864-6500

- Telephone the NASA STI Information Desk at 757-864-9658

- Write to:
  NASA STI Program
  Mail Stop 148
  NASA Langley Research Center
  Hampton, VA 23681-2199

A Numerical Study on the Effect of Facesheet-Core Disbonds on the Buckling Load of Curved Honeycomb Sandwich Panels

Evan J. Pineda, David E. Myers, Brett A. Bednarcyk, and Thomas M. Krivanek
Glenn Research Center, Cleveland, Ohio

Level of Review: This material has been technically reviewed by technical management.

Available from

A Numerical Study on the Effect of Facesheet-Core Disbonds on the Buckling Load of Curved Honeycomb Sandwich Panels

Evan J. Pineda, David E. Myers, Brett A. Bednarcyk, and Thomas M. Krivanek
National Aeronautics and Space Administration
Glenn Research Center
Cleveland, Ohio 44135

Abstract

A numerical study on the effect of facesheet-core disbonds on the post-buckling response of curved honeycomb sandwich panels is presented herein. This work was conducted as part of the development of a damage tolerance approach for the next-generation Space Launch System heavy lift vehicle payload fairing. As such, the study utilized full-scale fairing barrel segments as the structure of interest. The panels were composed of carbon fiber reinforced polymer facesheets and aluminum honeycomb core. The panels were analyzed numerically using the finite element method. Facesheet and core nodes in a predetermined circular region were detached to simulate a disbond induced via low-speed impact between the outer mold line facesheet and honeycomb core. Surface-to-surface contact in the disbonded region was invoked to prevent interpenetration of the facesheet and core elements. The diameter of this disbonded region was varied and the effect of the size of the disbond on the post-buckling response was observed. A significant change in the slope of the edge load-deflection response was used to determine the onset of global buckling and corresponding buckling load.

Introduction

The Space Launch Systems (SLS) payload fairing (PLF) is a key component of the next generation of heavy lift launch vehicles. The baseline design for the PLF involves separable honeycomb sandwich petals composed of aluminum honeycomb core and carbon fiber reinforced polymer (CFRP) facesheets. It serves to protect the vehicle payload from aerodynamic and acoustic loads during launch and must separate from the vehicle cleanly without re-contact. Pre-existing flaws, such as manufacturing defects or unexpected damage occurring during handling, assembly, payload encapsulation, and vehicle integration, can jeopardize the expected life and performance of the PLF. Typically, any damage initiated in the structure prior to launch will be repaired, if detected through visual inspection or non-destructive inspection (NDI). However, it is possible that some damage is undetected and does not get repaired, or impact damage may occur during flight. As such, the PLF must be damage tolerant.

Low-speed impact such as tool drops or unintended contact with ground support equipment, is the most prevalent cause of post-manufacturing damage. For honeycomb sandwich structures, low-speed impact results in core crushing, delamination/disbonds, and matrix cracking (Refs. 1 and 2). Subsequent loading can lead to kink band formation (fiber microbuckling), indentation (core crushing growth), and delamination/disbond growth (Refs. 1 to 4). It is essential to understand how the damage, ensuing from a low-speed impact, affects the performance of the PLF during launch, and to develop a suitable damage tolerance approach (DTA) for the 10.0 m diameter PLF that can be used to assess the critical flaw size and location and includes damage mitigation, inspection, and repair.

The PLF structure is designed to buckle before strength failure occurs and at a relatively low strain state. Therefore, due to the large size of the PLF acreage and the nature of the on-pad and aerodynamic loads, it is expected that buckling will remain the dominant mode of failure, even when there is damage present. A thorough experimental and numerical investigation of the buckling of 1/16th arc segments of the full-scale PLF barrel has previously been conducted by NASA for four different panel configurations (Refs. 5 to 9). Also contained in these papers is a study on the effect of geometric imperfections on the buckling response of the curved sandwich panels. Farrokh et al. (Ref. 10) investigated the effect of a joint,

and subsequent damage to the joint resulting from impact, on the buckling load of the curved panel segment. This work is complimentary to other NASA work related to cylindrical shell buckling knockdown factors (Refs. 11 to 13). In the current PLF designs, the resulting strength margins are typically high relative to the buckling margins. However, if it was determined that designs utilizing pristine strength allowables are not conservative enough to ensure that buckling occurs well before strength failure, the open hole or compression after impact (CAI) allowables could be utilized. Unfortunately, numerous additional coupon tests would be needed to develop the CAI allowables. However, CAI allowables have been developed for comparable systems used in the design of other structures, as this is the dominant mode of damage induced failure for these heavier loaded structures (Ref. 14). Results from these studies can be leveraged during the design phase of the PLF.

As mentioned previously, various damage mechanisms arise during impact and may evolve during service. Here, attention is focused only on the reduction in the overall buckling load of the PLF structure due to disbonding between the composite facesheet and honeycomb core resulting from a low speed impact. One reason for focusing on facesheet-core disbonds is that the tools necessary to perform the analysis have been extensively validated in the open literature and are integrated into commercially available software packages. Additionally, others have focused on CAI (Refs. 1 to 4, 14 and 15) and fatigue damage growth (Refs. 16 to 18) (as these modes are pertinent to those structures, which included the Ares I launch vehicle interstage, the Orion Multipurpose Crew Vehicle Stage Adaptor, and other hat-stiffened panels, and solid laminate skins) (Refs. 3, 14 to 18). Information and data from these studies are complimentary (as opposed to duplicative) to what will be obtained from this study. These results can be utilized to guide further development of a comprehensive DTA.

Herein, numerical analysis of 1/16th arc segments of the full-scale PLF barrel was conducted using the finite element method (FEM). The facesheet-core disbond was simulated by separating the facesheet nodes from the core nodes in a predetermined, circular, disbonded region. A surface-to-surface contact algorithm was utilized to eliminate interpenetration of the facesheet and core elements.

Previous authors utilized FEM analysis to calculate the strain energy release rate at a delamination front in post-buckled laminates (Refs. 19 and 20). Reeder et al. (Ref. 21) used a similar technique to investigate the effect of delamination growth on the post-buckling response of solid laminates using the virtual crack closure technique (VCCT) (Ref. 22). In addition, numerous authors have modeled the effect of core crushing on the CAI strength of honeycomb sandwich panels (Refs. 3, 4, and 15). However in the present work, the facesheet-core disbonds are not allowed to propagate, and core crushing is not considered in order to isolate the effect of the presence of a facesheet-core disbond on the post-buckling response of the panel. Geometrically nonlinear, post-buckling analysis was performed by incrementally applying a uniform edge displacement to the curved panel. The buckling load of the curved panel was determined by monitoring changes in the slope of the resulting load-deflection curve. A parametric study was conducted by varying the diameter of the disbonded region and the post-buckling response and buckling loads were compared to experimental and numerical data for pristine panels.

Buckling Test of Pristine Curved Sandwich Panel

To provide baseline data, a buckling experiment on a 3 by 5 ft section of a 1/16th arc segment of a 10 m diameter PLF honeycomb sandwich barrel section without a disbond (pristine) was conducted. The complete details and results for this test are available in previous work (Refs. 5 and 23).

The 1/16th fabrication demo panel was constructed on a concave composite tool (5 m radius of curvature) using an automated tape laying process. The pre-impregnated (pre-preg) tape was composed of unidirectional fibers and was 6 in. wide. The pre-preg contained IM7 fibers and 977-3 epoxy. The stacking sequence of the facesheets was [45°/90°/–45°/0°]s. The facesheets were bonded to the 1 in. thick aluminum core using FM 300 film adhesive, 0.08 lbs/ft^2. The aluminum honeycomb core was curved, via machining, to match the radius of the tool. The facesheets and core adhesive were co-cured in a single autoclave cycle. The aluminum core was Alcore PAA-CORE 5052, 0.0007 in. thick with 0.125 in. cell

size, with a density of 3.1 pcf. An adhesive splice was needed to join discontinuous sections of the core because the 1/16th barrel section panel dimensions exceeded the size of the pre-manufactured core. A core splice consisting of Hysol 9396.6 foaming adhesive was used to fill the gap between the two pieces of aluminum core.

One 3 ft wide by 5 ft long test specimen was machined from the manufacturing demo panel following non-destructive examination. End plates were employed in the testing. These were 1.0 in. thick aluminum plates and had a slot in the shape of the specimens cross section machined in the center. The slot width and length were such that, when centered, the specimen had a clearance of 0.5 in around the perimeter. After the specimen-end was centered in the slot and squared, it was potted with "UNISORB" V-100 epoxy grout. When both ends were potted and following cure, specimen ends were machined flat and parallel. The potted dimensions of the panel are shown in Figure 1. Note that the final dimensions of the gage section were not exactly 3 by 5 ft. The panel width dimension plotted in Figure 1 represents the average arc-length of the outer mold line (OML) and inner mold line (IML) facesheets. In addition to the overall dimensions, Figure 1 shows the relative position of the core splice with respect to the panel ends.

Once potted, strain gages were affixed to the OML and IML surfaces of the panel. These gages were monitored and the strains were recorded during loading of the panel. The panel was tested at the NASA Langley Research Center (LaRC) in a servo-hydraulic test frame. The panel was secured between two loading platens, with the bottom loading platen being fixed and the top platen allowed to move in the y-direction. The panel was loaded in compression until catastrophic failure occurred. Additional instrumentation included three direct-current displacement transducers (DCDTs) used to measure the global axial deformation of the panel, and a load cell attached to the load platen to measure the applied load. Finally, the panels were painted using a speckle pattern for photogrammetric measurements. Visual image correlation (VIC) was employed to obtain full-field strain measurements during the test as well as high-speed video.
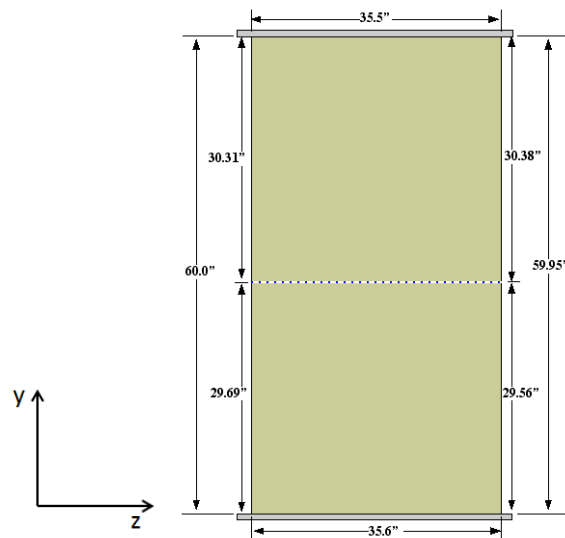

Figure 1.—Dimensions of pristine curved honeycomb
sandwich buckling test specimen with end plates.
Dashed line indicates core splice locations.

Determining the Buckling Load

Stable bifurcation of the panel can occur over a finite time (and applied edge displacement). Therefore, determining the buckling load of a panel from experimental data can be subjective. Various methods for determining the buckling load from experimental data is given in Singer et al. (Ref. 24). Ko (Ref. 25) compared the force/stiffness (F/S) method and the Southwell method for predicting the buckling strength of tubular panels. The original F/S method, developed by Jones and Greene (Ref. 26), used a stiffness (force divided by global strain) versus displacement plot to obtain the buckling load.

In the present work, the F/S method was utilized to calculate the buckling load from both the tests and analysis. The stiffness measure used was taken to be the applied load P divided by displacement U (the average of all three DCDT measurements for the experimental value, or the end shortening for the numerical values). Rather than plot this stiffness measure against load, the normalized stiffness P/U versus displacement curves were generated, as shown Figure 2. Referring to Figure 2, it can be observed that there is some initial settling in the test; after which, the critical buckling load P_{cr} is taken as the load at which the relationship between the decreasing stiffness and applied load becomes linear. This is marked by the intersection of a nearly vertical dashed line with the F/S curve on Figure 2 and corresponds to 75.6 kips.

Note that the method used in this work varies slightly from the original F/S method (Ref. 26). In the original method, P_{cr} is taken as the load when the F/S curve crosses the load axis. However, this is well into the post-buckled regime. If there is local failure or instability, Jones and Greene (Ref. 26) recommend using the point of intersection of a straight line with the F/S curve to determine the buckling load. The slope of the straight line is obtained from the critical strain required to initiate local failure. For these analyses, this limiting strain was unknown. As mentioned before, these methods (as well as other methods in the literature) contain some bias. The method used in this work is no different, but as long as a consistent method is used to calculate the P_{cr} for all cases, comparisons can be made. For the datasets obtained from the experiment and generated from the FEM simulations, the described method provided the most consistent results with the least ambiguity.
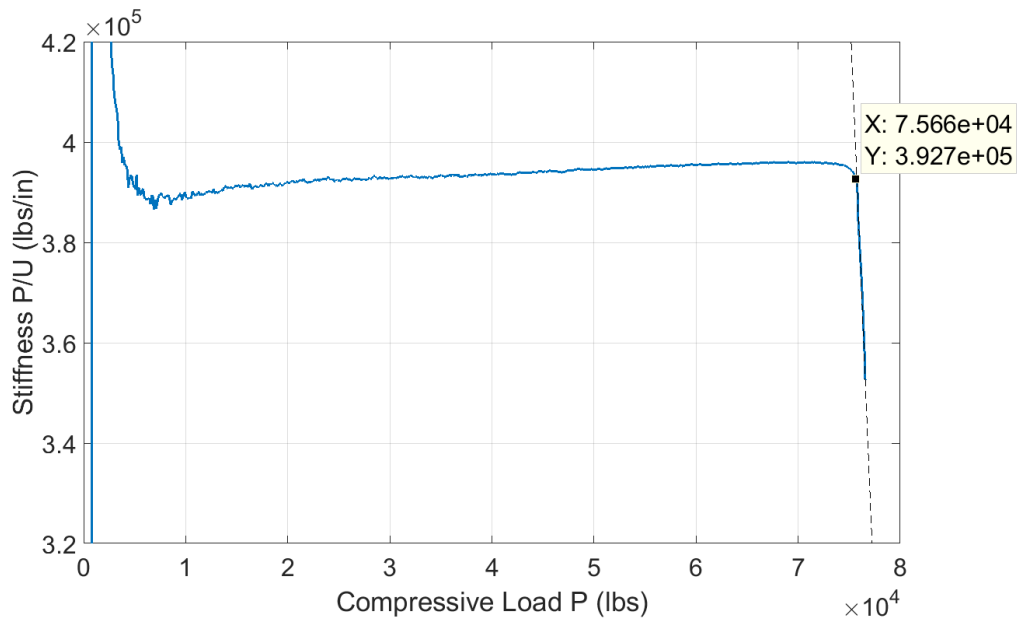

Figure 2.—F/S curve of experiment showing edge load/displacement P/U versus compressive load P.

Numerical Post-Buckling Analysis of Curved Sandwich Structures Containing Static Disbonds

The post-buckling response of 3 by 5 ft. sections of 1/16th arc segments of a 10.0 m diameter PLF honeycomb sandwich barrel section, with and without facesheet-core disbonds, was conducted using the Abaqus/Standard FEM package (Ref. 27). The facesheets consisted of 8-ply, IM7/977-3 CFRP composite laminates with a [45°/90°/–45°/0°]s stacking sequence. The elastic properties for IM7/977-3 were obtained from the Orion materials database. The elastic properties for the aluminum (5052-T6 alloy), 3.1 pcf, honeycomb core were obtained from commercially available datasheet provided by Alcore and are presented in Table I.

The honeycomb core was modeled using reduced-order, quadratic solid elements (C3D20R) and the facesheets were modeled using reduced-order quadratic shell elements (S8R). The facesheets were attached to the core via tie constraints to allow for dissimilar meshes for the cases where a disbond was present. From previous analyses, including the experimental end fixtures in the model was deemed non-critical. Thus, they were omitted from these models. A uniform, compressive edge displacement in the y-direction (see Figure 1) was applied to all nodes on the top edge of the panel, all other degrees of freedom (DOFs) on the top edge nodes were constrained, and the DOFs of all nodes on the bottom edge of the panel were constrained to simulate typical buckling experiment boundary conditions. The implicit dynamic FEM solver, along with geometric non-linearity, in Abaqus were used for the progressive collapse (post-buckling) simulations. A realistic displacement rate of 3.0E-4 in./s was used.

The FEM geometry and mesh used to model the pristine panel are presented in Figure 3. The geometry was created based on the gage dimension given in Figure 1, such that the average of the arc lengths of the OML and IML facesheets was 35.5 in. The core splice shown in Figure 1 was not included in the FEM model. A global seed, which controlled the size of the elements, of 1 in. was used to create the meshes for the core and facesheets. One element was used through the thickness in the core for all analyses in this work. In addition to the post-buckling analysis, a linear eigenvalue analysis was performed.

To simulate damage resulting from low-speed impact, a circular disbond with diameter D, was placed between the core and the inner surface of the OML facesheet. The FEM geometry, displaying a typical facesheet-core disbond is shown in Figure 4. The disbond area on the outer surface of the core and inner surface of the OML (highlighted in red) were not tied. Instead, surface to surface contact interaction was used with frictionless, finite sliding and a "hard" pressure-overclosure relationship. The penalty method was used as the constraint enforcement method (Ref. 27). The inner OML and outer core surfaces outside of the disbonded area (shown in gray in Figure 4) are still attached through a tie constraint, as are the entire outer IML and in inner core surfaces because there is no disbond between these surfaces. A demonstrative FEM mesh for a panel containing a 5 in. diameter disbond is presented in Figure 5. A global seed of 1 in. is still utilized. However, the meshes for the core and OML facesheet differ from the pristine model (Figure 3) because of the circular shape of the disbonded area. The IML facesheet remains the same as in Figure 3.

TABLE I.—ELASTIC PROPERTIES FOR
ALUMINUM HONEYCOMB CORE

Property, units	Value
E_x, ksi	75
E_y, psi	21.28
E_z, psi	21.28
v_{xy}	1.0E-05
v_{xz}	1.0E-05
v_{yz}	0.33
G_{xy}, ksi	22
G_{xz}, ksi	45
G_{yz}, psi	5.32
ρ, pcf	3.1

The diameter of the disbonded area was parametrically reduced in this study (i.e., disband diameter decreased from 20 to 5 in., typically in 5 in. increments), post-buckling analyses were conducted, and the buckling loads calculated using the method described in the previous section. Disbonds below 5 in. diameter were not considered, since diameters smaller than 5 in. had very little effect on the critical buckling load and global buckling mode (presented in the next section). Secondly, smaller disbonds would have required a finer mesh in the disbonded region, which would have yielded inconsistent mesh densities for simulations with disbonds smaller than 5 in. in diameter as compared to those greater than or equal to 5 in.
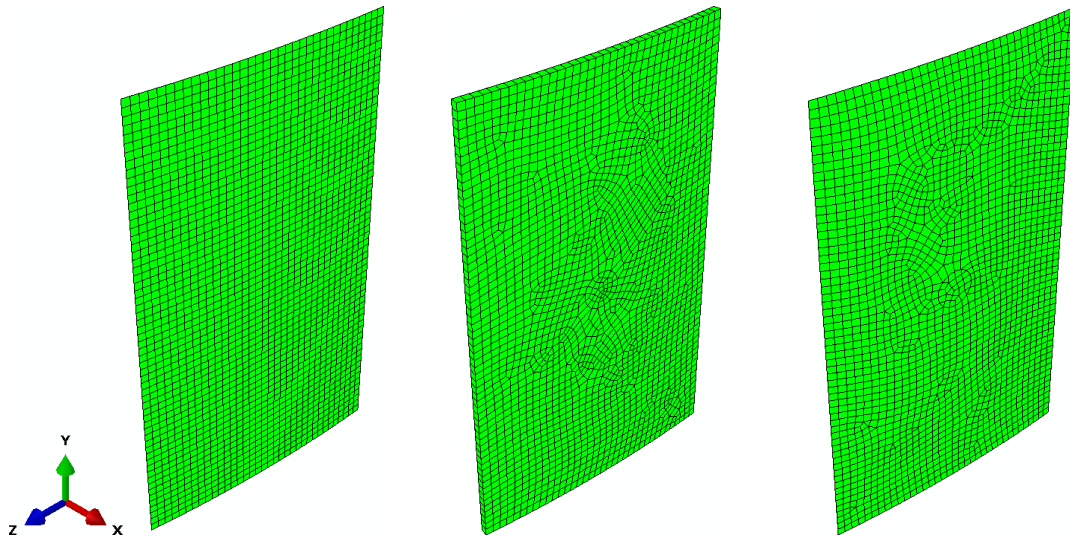

Figure 3.—FEM meshes used in numerical analysis of pristine curved honeycomb sandwich panel. Left: FEM mesh of IML facesheet composed of S8R, reduced-order shell elements. Middle: FEM mesh of honeycomb core composed of C3D20R, reduced-order solid elements. Right: FEM mesh of facesheets composed of S8R, reduced-order shell elements.
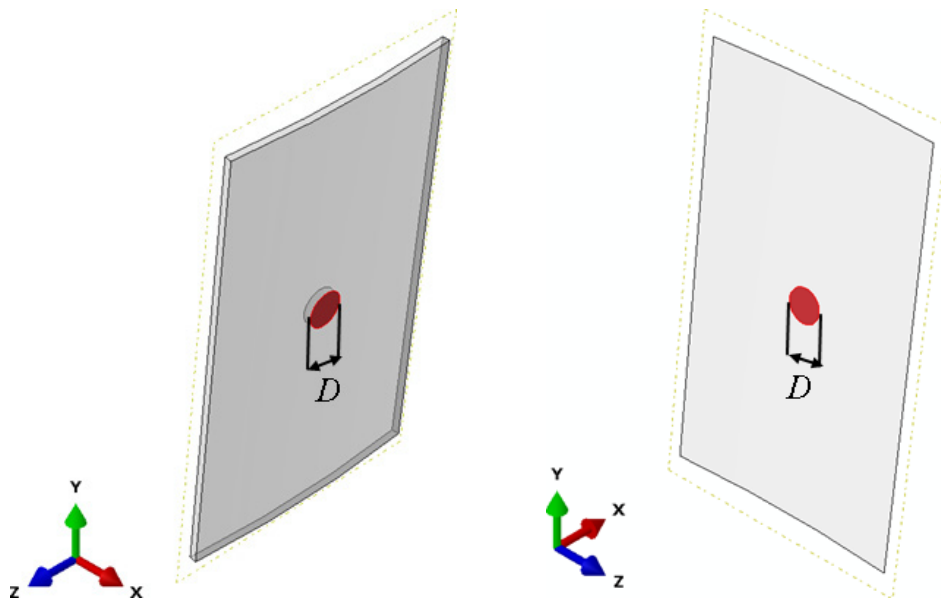

Figure 4.—FEM geometry of curved honeycomb sandwich panel showing disbonded area (D = 5 in.) between OML facesheet and core highlighted in red. Left: Honeycomb core geometry. Right: OML facesheet geometry.
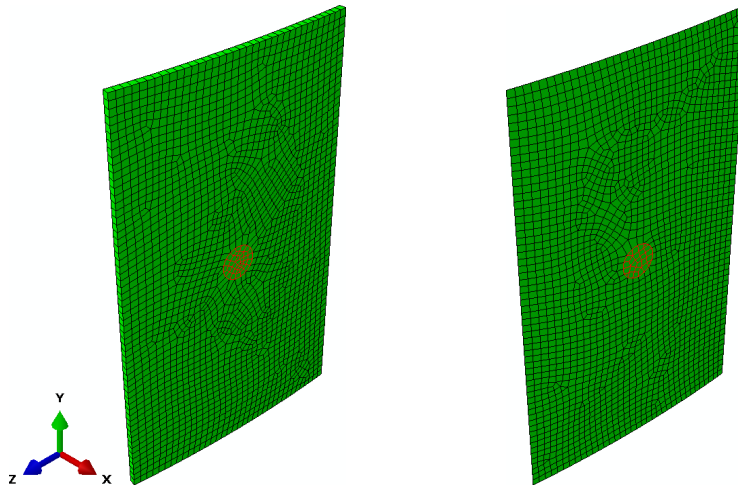
Figure 5.—FEM mesh used in simulations of curved honeycomb sandwich panels containing facesheet core disbond (*D* = 5 in.). Disbonded area highlighted in red. Left: Honeycomb core mesh. Right: OML facesheet mesh. Note, IML facesheet mesh remains the same as that shown in Figure 3.

Results

Pristine Panel

Critical Buckling Load

Figure 6 shows the F/S curve from the pristine post-buckling analysis, as compared to experiment. It can be inferred from Figure 6 that critical buckling load, predicted by FEM, was 71.4 kips. This prediction was conservative and exhibiting a 5.6 percent error from the experimental value. The linear eigenvalue for this panel was calculated to be 0.19 and the corresponding buckling load was 77.4 kips (2.3 percent error). It should be noted that including geometric imperfections has been shown to improve the post-buckling results for this panel (Refs. 5 and 9). Such imperfections were not considered herein.

Buckling Mode

The buckling mode (post-buckled shape) of the pristine panel predicted using a linear eigenvalue analysis, post-buckling analysis, and obtained from the VIC of the experiment is displayed in Figure 7. The radial displacement of the IML surfaces of the panels are shown in Figure 7. Blue/purple indicates displacement toward the positive *x* (or OML) direction (out of the page), whereas red indicates displacement towards the IML (into the page). With the linear eigenvalue analysis, the direction in which the eigenvectors are applied is arbitrary. The VIC data shows the panel buckling towards the IML, but the direction of buckling predicted by the post-buckling analysis was incorrect (opposite). It has been shown that geometric imperfections are required to get the correct buckling direction in a post-buckling analysis for this panel, and the buckling load is marginally dependent on the buckling direction and degree of imperfection (Refs. 5 and 9).
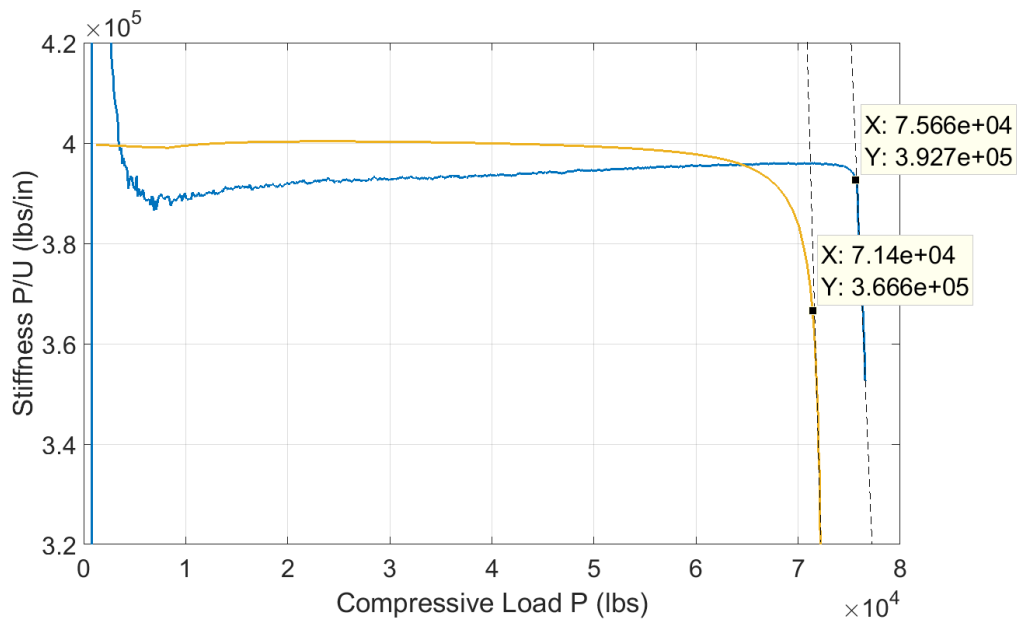
Figure 6.—F/S curves showing edge load/displacement *P/U* versus compressive load *P* from post-buckling simulation of pristine panel compared to experiment.
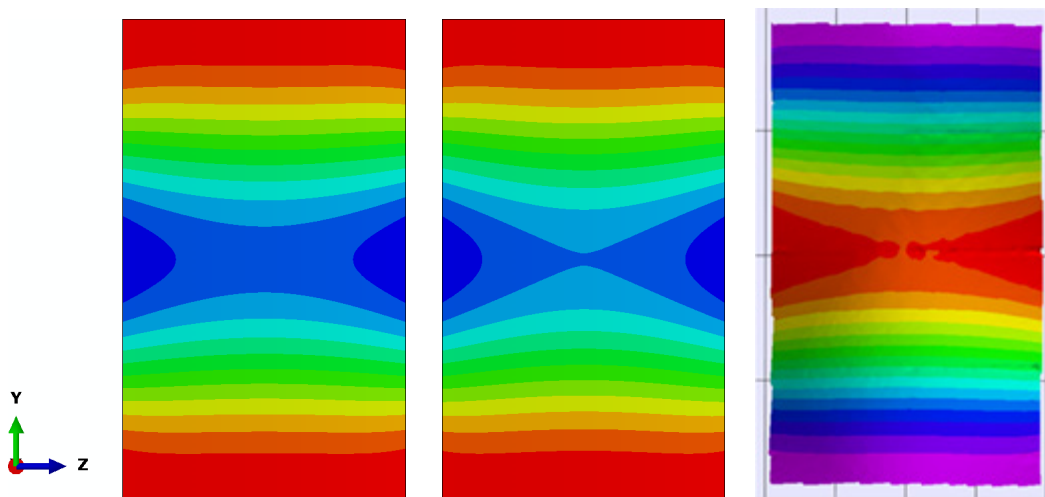

Figure 7.—Post-buckled view of radial displacement IML surface curved honeycomb sandwich panels. Left: Eigenvalue analysis. Middle: Post-buckling analysis. Right: Experimental VIC.
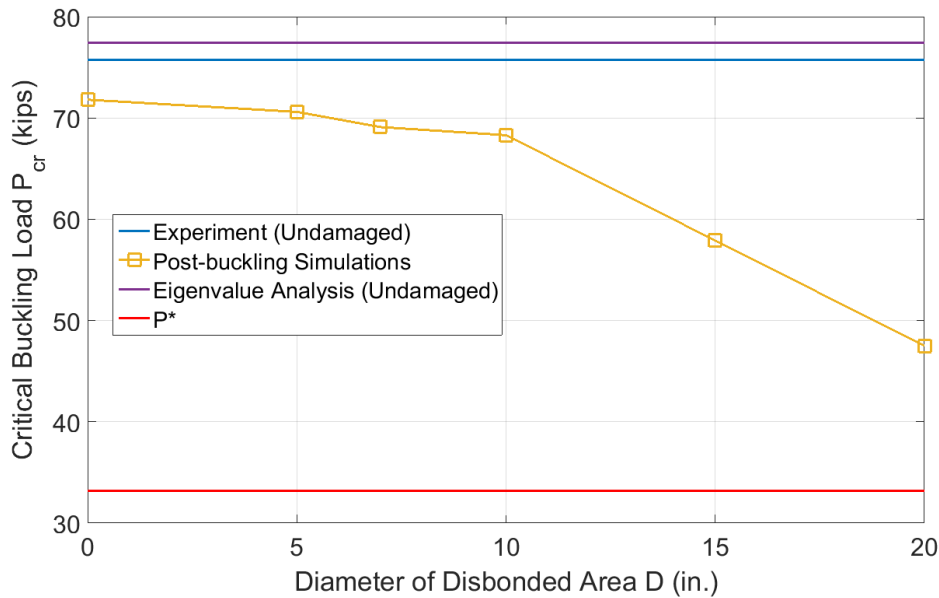
Figure 8.—Critical buckling load P_{cr} versus diameter of circular disbonded D area predicted by post-buckling FEM simulations. P^* is the design-to buckling load based on the linear eigenvalue, a safety factor of 1.4, and a shell buckling knockdown factor of 0.65.

Damaged Panel

Critical Buckling Load

A plot of critical buckling load versus disbonded area obtained from the progressive collapse simulations is displayed in Figure 8. It can be observed that the presence of even a 5 in. diameter disbond affected the buckling load, albeit slightly (1.6 percent reduction in critical load). The influence of a 10 in. diameter disbond was more pronounced and yielded nearly a 5 percent reduction in P_{cr}. As expected, the critical buckling load continued to decrease as the disbonded area was increased. However, it should be mentioned that the energy required to create a 10 in. diameter disbond is extremely high, and would most likely result in visible surface damage. Thus, damage resulting from this level of impact would be detected and repaired. For comparison, the buckling load from the experiment and from the linear eigenvalue analysis are plotted on Figure 8.

Typical aerospace designs utilize a factor of safety (*FS*) (Ref. 28). In addition, design-to loads for shell buckling also include a shell-buckling knockdown factor (*SBKF*) since buckling is extremely sensitive to a plethora of imperfections (Ref. 29). The margin of safety (*MS*) is calculated using the *FS* and *SBKF*

$$MS = \frac{\lambda_{cr} * SBKF}{FS} - 1 \tag{1}$$

where λ_{cr} is the linear eigenvalue obtained from analysis. From this equation the maximum applied load P^* allowed to meet *SBKF* and *FS* requirements based on the current design, can be calculated

$$P^* = P_{cr}^\lambda \left(\frac{SBKF}{FS} \right) \tag{2}$$

where P_{cr}^{λ} is the buckling load obtained from the linear eigenvalue analysis. Using typical values (*FS = 1.4* and *SBKF* = 0.65 (Refs. 28 to 29)) *P** for the pristine panel was calculated and plotted (red line) on Figure 8. It can be readily seen the buckling loads of the damaged panels (even for the maximum damaged area of 20 in. in diameter) do not approach *P**. Furthermore, a 5 in. diameter damage zone is well within the detectable range of modern non-destructive evaluation (NDE) techniques, and would be repaired upon inspection. This indicates that the *SBKF* is severely conservative with respect to damage, and previous work by Pineda et al. (Ref. 9) has shown similar findings regarding geometric imperfections. Although, these studies have not been performed on full cylinders, they support the efforts led by the NASA Langley Research Center to formulate a new, more physics-based *SBKF* to provide more design flexibility, and ultimately weight savings (Refs. 11 to 13).

Stiffness

The stiffness of the panels $\left.\dfrac{P}{U}\right|_{U=0.1}$ used in each simulation was calculated by dividing the applied compressive load evaluated at a displacement U of 0.1 in. The degradation in stiffness as a function of disbond size, along with stiffness of undamaged test panel, is given in Figure 9. The predicted stiffness of the pristine panel was 399 kips/in., which was 1.6 percent greater than the actual stiffness of the panel (394 kips/in.). Figure 9 illustrates that the presence of a disbond has a noticeable effect on the stiffness of the panel. It is possible that this information could be used to detect disbonds or other damage in these panels.
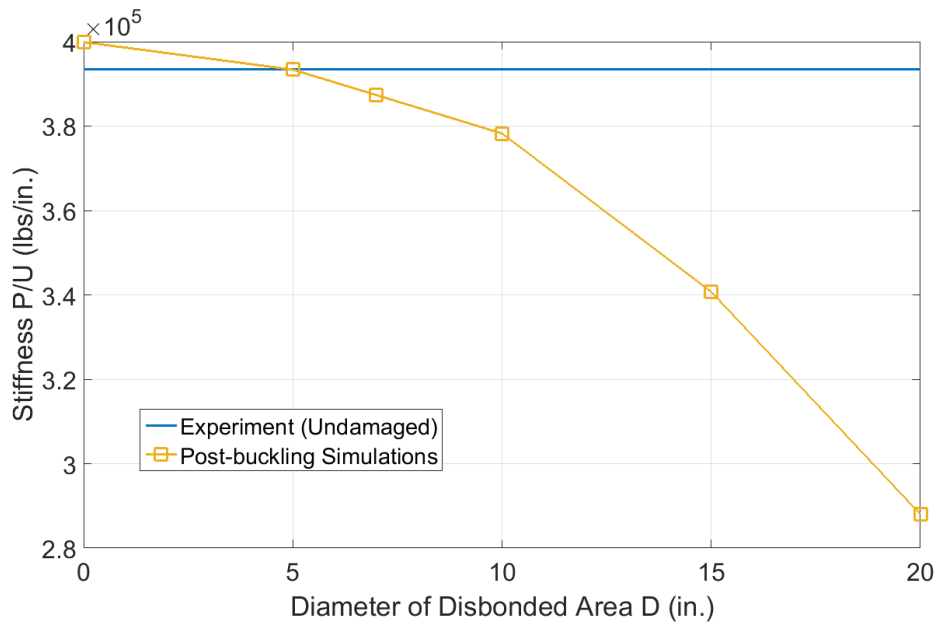

Figure 9.—Stiffness evaluated at 0.1 in applied displacement $\left.\dfrac{P}{U}\right|_{U=0.1}$ versus diameter of disbonded area *D* from FEM simulations. Stiffness from experiment on undamaged panel is also displayed for comparison.
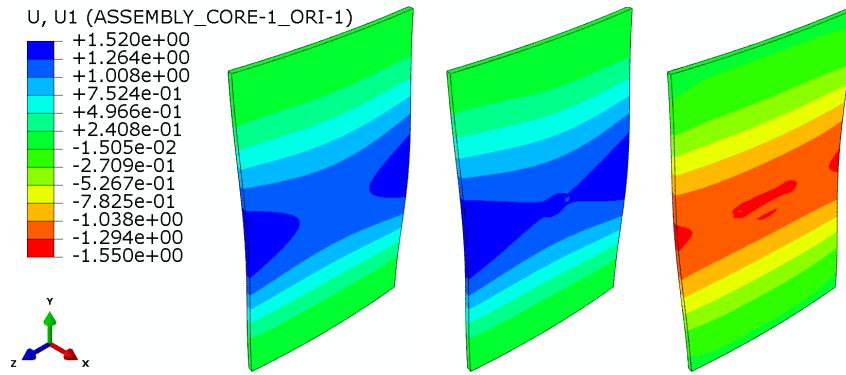
Figure 10.—Global buckling modes predicted with FEM. (Left). No damage.
(Middle). Diameter of disbond *D* = 5 in. (Right). Diameter of disbond *D* = 10 in.

Buckling Mode

The post-buckled shapes for the undamaged, $D = 5$ in., and $D = 10$ in. are presented in Figure 10 and the radial displacement contours are plotted on the deformed shapes. The buckling direction of the $D = 5$ in. panel was towards the OML, which is the same as the undamaged prediction, but opposite the experiment. The out-of plane (radial) displacement of the $D = 5$ in. panel differs slightly from the pristine panel, and the disbonded area is apparent in the displacement field contour. With a disbond diameter of 10 in. (left contour in Figure 10), the buckling direction switches towards the IML (as in the experiment), and facesheet wrinkling can be observed in the damage zone.

Figure 11 shows the progression of radial displacement (as a color contour) and the deformed shape, locally in the disbonded area obtained from the post-buckling simulation with a damaged area diameter of 5 in. Not that the color scales for the contours in Figure 11 are not the same from one load level to the next. On the left, the ratio of the current load P to critical buckling load P_{cr} is given. Early in the simulation, at 26 percent of the buckling load, the facesheet started to indent the core, and the local wrinkling mode exhibited a half wave shape in each direction. It was not until the load reached 88 percent of P_{cr} that the local mode transitioned to a full wave in the *y*-direction (height), and facesheet and core start to separate slightly (the displacement contours of the facesheet and core show some small variation). At 99 percent of P_{cr} the local winkling mode began transitioning towards a 1.5 wave shape, and the core has lost contact with the facesheet in a significantly large area. Finally in the post-buckled regime (101 percent of P_{cr}) there is substantial loss of contact between the core and facesheet. The core has displaced noticeably towards the IML in a 1.5 wave shape, while the OML facesheet remains comparatively flat.

Similar plots are given in Figure 12 for the case of a 10 in. disbond, $D = 10$ in. Resembling the local deformation evolution of $D = 5$ in., the facesheet and core displaced into a half wave shape at 7 percent of the buckling. At 59 percent of the buckling load, the core and facesheet transitioned directly into a 1.5 wave shape, yet contact was lost in the regions surrounding the peaks of the wave shape. The facesheet and core separated substantially at 97 percent of the buckling load. Finally at the buckling load, the facesheet remained in a 1.5 wave shape while the core deformed into a shape close to a half wave. Facesheet-core contact only persisted at the boundaries of the disbonded areas and the center of the panel. It can also be seen from Figure 12 that the separation between the facesheet and core progresses much faster, relative to P_{cr}, than when $D = 5$ in.
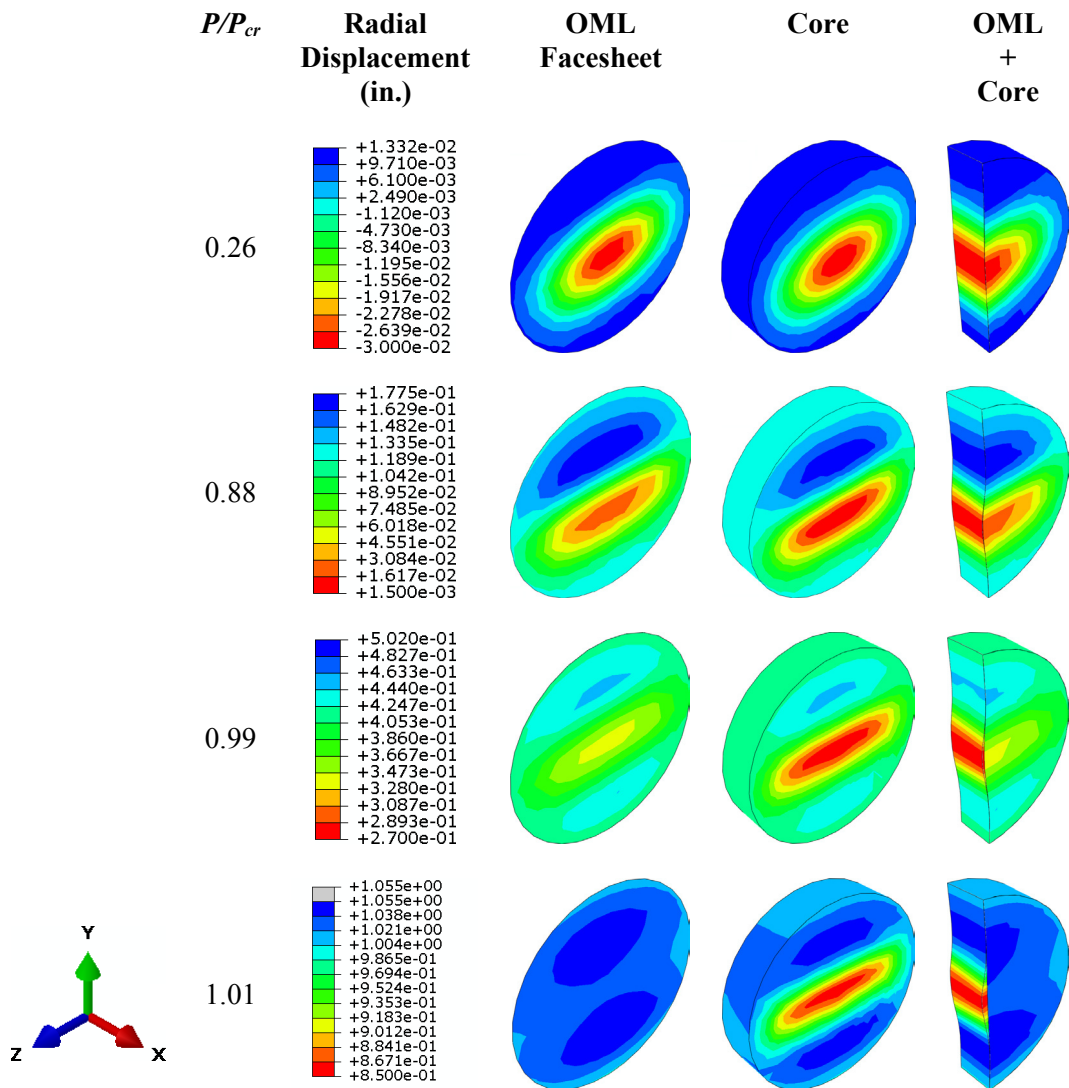
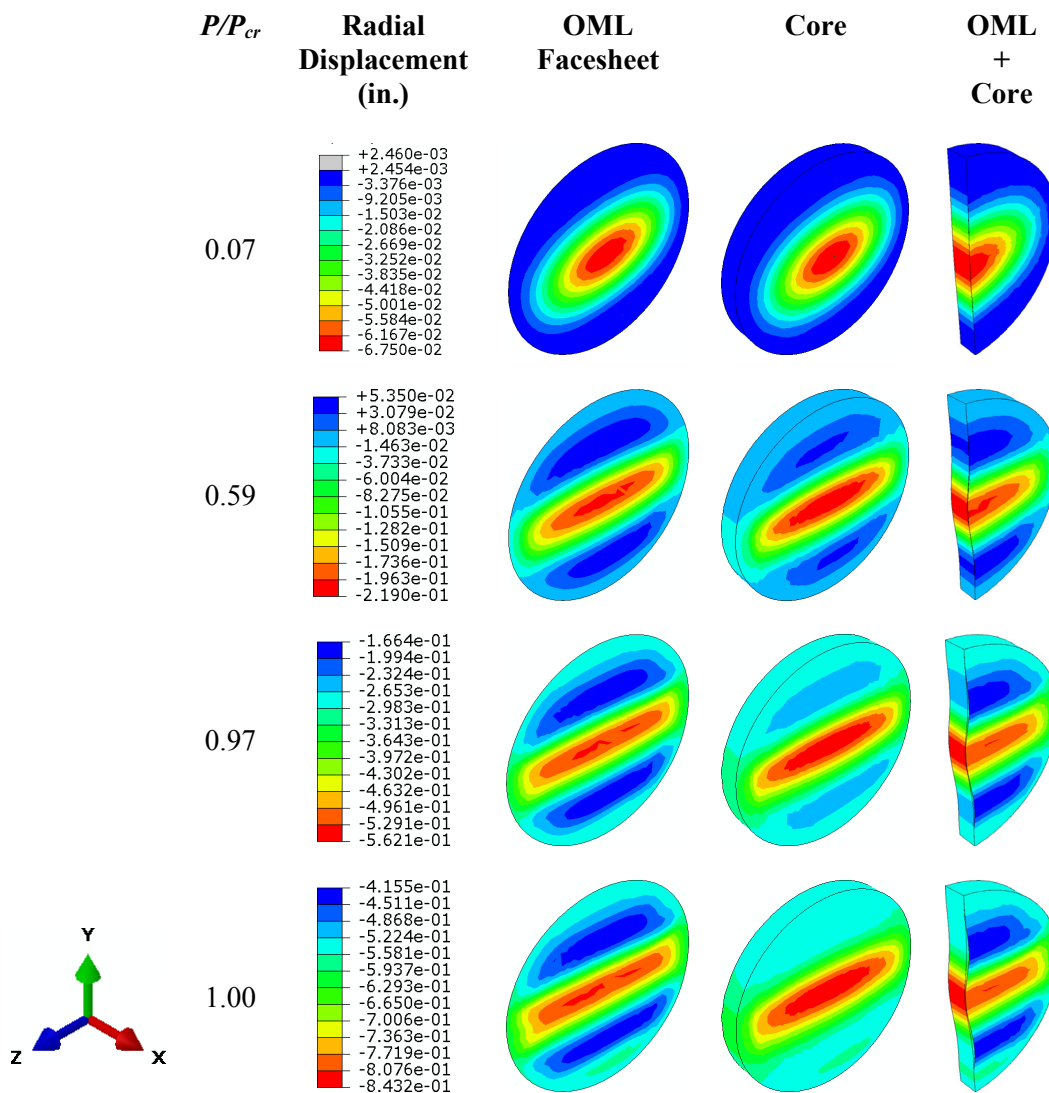Figure 11.—Local facesheet wrinkling in disbonded zone with diameter D = 5 in.

Figure 12.—Local facesheet wrinkling in disbonded zone with diameter *D* = 10 in.
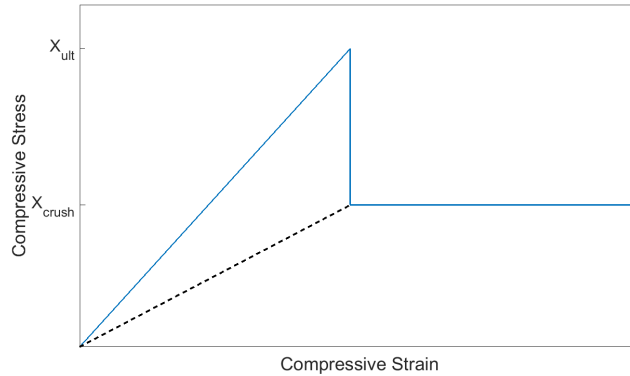
Figure 13.—Representation of compressive response of aluminum honeycomb core. X_{ult} is the compressive core ultimate strength, and X_{crush} is the core crush strength.

Core Crushing

As mentioned in the introduction, another mechanism that may arise in a honeycomb sandwich panel, besides debonding of the core and facesheet, is core crushing. This may occur as a result of the impact causing the damage or subsequently when the facesheet starts wrinkling (local buckling and pressing on the core). The idealized stress-strain response of the honeycomb core is given in Figure 13 (Refs. 1 to 4). The core behaves linearly until X_{ult} is exceeded, as indicated with the blue line. After which, the core is crushed and the stress drops rapidly to X_{crush}. Subsequent loading results in perfectly plastic deformation. After the core is crushed, the elastic stiffness of the core is reduced, marked by the dashed black line. Any elastic unloading and reloading will follow this path until the X_{crush} is achieved. Then, the core will resume perfectly plastic behavior.

The through-thickness, compressive stress in the core for the undamaged panel did not exceed X_{ult} and only surpassed X_{crush} well into the post-buckled regime and only locally in a region near the potted ends of the panel. The end fixtures were not included in these models; however, it is expected that the potting would alleviate these stresses and core crushing would not be an issue for the pristine panel. Moreover, no core crushing was observed after the buckling test on the undamaged panel.

Nonlinear behavior in the core (as shown in Figure 13) was not included in the model. However, Figure 14 contains plots of the applied load when the through thickness, compressive stress at an integration point in a core element first exceed the core allowables as a function of disbond size. The blue line containing "*" markers represents the applied load at which the compressive stress in the core first exceed X_{ult}, and the purple line with "x" markers shows what the applied load was when the compressive stress in the core was first above X_{crush}. For reference, the non-linear buckling load P_{cr} as a function of disbond diameter and the knocked down linear eigenvalue load $P*$ for the pristine panel are also presented in Figure 14.

It can be seen that X_{ult} is not exceeded until the buckling load is exceeded, or very near the buckling load (within 10 percent) for all cases. Most likely, a controlled validation test for this analysis would involve placing a Teflon insert between the OML facesheet and core prior to adhering the facesheet to the core. Thus, based on Figure 14, core crushing should not be a concern.

However in a "real-world" scenario, impact would be primary the causes of the disbond and could result in core crushing. It can be inferred from Figure 14 that, with the current panel design, it is possible that the applied loads would surpass the load necessary to induce a nonlinear response in pre-crushed core.

It is not apparent what influence on the overall structure local core crushing will have or to what extent the core crushing would evolve. Furthermore, if the core is crushed during the impact event itself, the facesheet may also have a change in morphology due to damage, and the local facesheet wrinkling mode that occurs during subsequent axial loading might change and/or may not exert large enough stresses on the pre-crushed core to result in further core crushing.
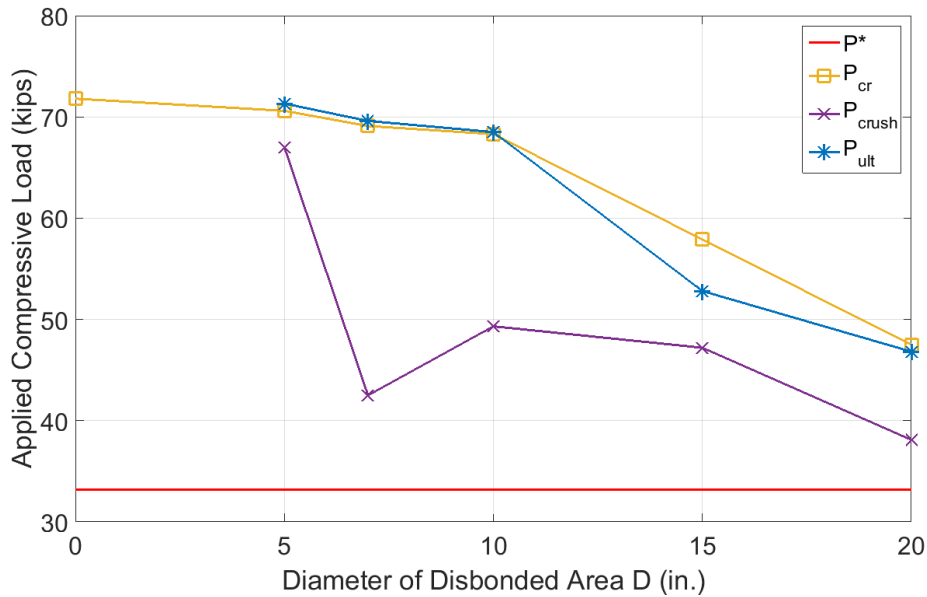
Figure 14.—Applied load at which the local through-thickness stress at an integration
point in a core element first exceeds the core crush ultimate strength (305 psi) P_{ult}
and core crush allowable (145 psi) P_{crush} as a function of disbond size. Predicted
buckling load from post-buckling analysis P_{cr} and knocked down (by *FS* and *SBKF*)
buckling load from eigenvalue analysis *P** also plotted for comparison.

Moreover, the large stresses in the core may only be a facet of the mesh-dependent stress concentration induced in the model at the disbond fronts. The core crush allowable was exceed at integration points in elements that were near the boundary of the disbonded zone, or the crack front, where the gradients are very steep. This mesh dependence may be why the panel with the 7 in. diameter disbond exhibited a lower load necessary to induce local core crushing than the panels containing 10 in. or 15 in. diameter disbonds, as observed in Figure 14.

Lastly, it may be possible that not all of the core in the disbonded region has crushed. Thus, using the ultimate core strength (305 psi) to indicate core crush initiation may have been more appropriate.

Higher fidelity analysis, including better mesh refinement near the disbond boundary, or physical testing, is needed to assess if core crushing prior to buckling is a realistic concern. To model the mathematical singularity appropriately, elements containing double nodes at the crack front are needed. It may be possible to capture the stresses surrounding the crack front accurately by including cohesive zone elements in the models (Refs. 27, 30, and 31). If core crushing does affect the buckling response of the panel, a non-linear constitutive model incorporating core crushing behavior can be included (Ref. 3), but a non-local consideration of stress in the vicinity of the crack front may be necessary due to the mathematical singularity. Furthermore, the evolution of the disbonded area can be included through the use of VCCT or cohesive zone elements. Future work will focus on developing models that encompass these mechanisms.

Facesheet Failure

The Tsai-Hill failure criterion (Ref. 32) was used to predict potential facesheet strength failure during the progressive collapse simulation. B-Basis stress allowables from the Orion database were used in the criterion. The failure criterion was satisfied after the panel had buckled for the cases considered. This would indicate that facesheet failure, which could be due to mechanisms such as matrix cracking, or fiber microbuckling (kink band formation), may not influence the buckling load of the impact damaged panel, and may not be a primary concern. However, it is still possible that damage induced during the impact serves as a nucleation site for premature damage growth during subsequent loading.

Conclusions

The effect of impact damage on a large curved honeycomb sandwich structures was idealized as a disbond between the CFRP facesheet and aluminum honeycomb core. The panel segments considered are part of 10 m diameter SLS payload fairing barrel section. Since the design of the fairing is driven by failure due to buckling, not strength, the influence of the presence of a disbond on the buckling load of the panel was of primary concern.

The FEM was used to investigate the effect of disbonds on the buckling load of 3 by 5 ft segments of the fairing barrel section. Circular disbonded regions were simulated by separating the nodes of the facesheet from the core and utilizing a surface-to-surface contact relationship in this region. In a parametric study, the diameter of the disbonded zone was varied from 5 to 20 in. Progressive collapse simulations were performed to predict the post-buckling response of the panels containing disbonds. The results from the post-buckling analysis were compared to experimental test data for a pristine (undamaged) panel and linear eigenvalue buckling load predictions.

The analysis results indicated that a disbond with a diameter of 10 to 15 in. (which is well within the detectable range of NDE techniques) would be required before the buckling load of the panel was decreased substantially (> 20 percent). Moreover, a factor of safety (*FS*) and a shell buckling knockdown factor (*SBKF*) is used when stiffness-driven curved shell structures are designed. The analysis predicted that a disbond greater than 20 in. in diameter would be required to violate the *FS* and *SBKF*.

The global buckling mode of the panels appeared insensitive to the presence of the disbond. However, local buckling, or wrinkling of the facesheet was observed when there was a disbond greater than 5 in. Moreover, the predicted direction of buckling switched from towards the OML to towards the IML when the disbonds were greater than or equal to 10 in. in diameter.

The local facesheet wrinkling induced larger compressive stresses at integration points within core elements that were at the boundary of the disbond, or crack front. These stresses exceed the core crushing ultimate compressive allowable, provided by the vendor, prior to buckling, indicating that core crushing may possibly effect the buckling response of the panel. However, local failure of the facesheets, due to strength failure, did not appear to be a prevalent issue.

Future work will involve, the utilization of finer meshes, along with crack tip elements or cohesive elements to capture the stress concentrations at the disbond boundary that could affect the core crushing. In addition, core crushing can be incorporated into the model through the use of a non-linear constitutive model for the core, and disbond growth can be captured through VCCT or with cohesive zone elements.

References

1. Raju, K.S., B.L. Smith, J.S., Tomblin, K.H. Liew, and J.C. Guarddon. 2008. "Impact Damage Resistance and Tolerance of Honeycomb Core Sandwich Panels," *J. Compos. Mater.*, 42(4): 385-412.
2. McQuigg, T.S., R.K. Kapania, S.J. Scotti, and S.P. Walker. 2012. "Compression After Impact on Honeycomb Core Sandwich Panels with Thin Facesheets, Part 1: Experiments," presented at the 53rd AIAA/ASME/ASCE/AHS/ASC Structures, Structural Dynamics, and Materials Conference, April 23-26, 2012, Honolulu, Hawaii.
3. Ratcliffe, J.G., and W.C. Jackson. 2008. "A Finite Element Analysis for Predicting the Residual Compressive Strength of Impact-Damaged Sandwich Panels," *NASA/TM—2008-215341*.
4. Lacy, T.E., and Y. Hwang. 2003. "Numerical Modeling of Impact-Damaged Sandwich Composites Subjected to Compression-After-Impact Loading," *Compos. Struct.*, 61: 115-128.
5. Myers, D.E., E.J. Pineda, B.F. Zalewski, D.N. Kosareo, and S. Kellas. 2013. "Buckling Testing and Analysis of Honeycomb Sandwich Panel Arc Segments of a Full-Scale Fairing Barrel, Part 1: 8-Ply In-Autoclave Facesheets," *NASA/TM—2013-217822/PART1*.

6. Pineda, E.J., D.E. Myers, D.N. Kosareo, B.F. Zalewski, and G.D. Dixon. 2013. "Buckling Testing and Analysis of Honeycomb Sandwich Panel Arc Segments of a Full-Scale Fairing Barrel, Part 2: 6-Ply In-Autoclave Facesheets," *NASA/TM—2013-217822/PART2*.

7. Pineda, E.J., D.E. Myers, D.N. Kosareo, and S. Kellas. 2014. "Buckling Testing and Analysis of Honeycomb Sandwich Panel Arc Segments of a Full-Scale Fairing Barrel, Part 3: 8-Ply Out-of-Autoclave Facesheets," *NASA/TM—2013-217822/PART3*.

8. Myers, D.E., E.J. Pineda, D.N. Kosareo, and G.D. Dixon. 2015. "Buckling Testing and Analysis of Honeycomb Sandwich Panel Arc Segments of a Full-Scale Fairing Barrel, Part 4: 6-Ply Out-of-Autoclave Facesheets," *NASA/TM—2013-217822/PART4*.

9. Pineda, E.J., D.E. Myers, D.N. Kosareo, B.F. Zalewski, S. Kellas, G.D. Dixon, T.M. Krivanek, and T.G. Gyekenyesi. 2014. "Buckling Testing and Analysis of Honeycomb Sandwich Panel Arc Segments of a Full-scale Fairing Barrel: Comparison of In- and Out-of-Autoclave Facesheet Configurations," presented at the 55th AIAA/ASME/ASCE/AHS/ASC Structures, Structural Dynamics, and Materials Conference, January 12-19, 2014, National Harbor, Maryland.

10. Farrokh, B., K.N. Segal, S. Kellas, S.M. Akkerman, R.L. Glenn, E.J. Pineda, B.T. Rodini, and W.M. Fan. 2014. "Buckling of Longitudinally Jointed Curved Composite Panel Arc Segment for Next Generation of Composite Heavy Lift Launch Vehicles: Verification Testing and Analysis," present at the *CAMX – The Composites and Advanced Materials Expo*, 13-16 October 2014, Orlando, Florida.

11. Haynie, W.T., M.W. Hilburger, M. Bogge, M. Maspoli, and K. Benedikt. 2012. "Validation of Lower-Bound Estimates for Compression-Loaded Cylindrical Shells," presented at the 53rd AIAA/ASME/ASCE/AHS/ASC Structures, Structural Dynamics, and Materials Conference, April 23-26, 2012, Honolulu, Hawaii.

12. Hilburger, M.W. 2012. "Developing the Next Generation Shell Buckling Design Factors and Technologies," presented at the 53rd AIAA/ASME/ASCE/AHS/ASC Structures, Structural Dynamics, and Materials Conference, April 23-26, 2012, Honolulu, Hawaii.

13. Kriegesmann, B., M.W. Hilburger, and R. Rolfes. 2012. "The Effects of Geometric and Loading Imperfections on the Response and Lower-bound Buckling Load of a Compression-Loaded Cylindrical Shell," presented at the 53rd AIAA/ASME/ASCE/AHS/ASC Structures, Structural Dynamics, and Materials Conference, April 23-26, 2012, Honolulu, Hawaii.

14. Nettles, A.T., and J.R. Jackson. 2009. "Developing a Material Strength Design Value Based on Compression After Impact Damage for the Ares I Composite Interstage," *NASA/TP—2009-215634*.

15. McQuigg, T.S., R.K. Kapania, S.J. Scotti, and S.P. Walker. 2012. "Compression After Impact on Honeycomb Core Sandwich Panels with Thin Facesheets, Part 2: Analysis," presented at the 53rd AIAA/ASME/ASCE/AHS/ASC Structures, Structural Dynamics, and Materials Conference, April 23-26, 2012, Honolulu, Hawaii.

16. Bisagni, C., C.G. Dávila, C.A. Rose, and J.N. Zalameda. 2014. "Experimental Evaluation of Fatigue Damage Progression in Postbuckled Single Stringer Composite Specimens," presented at the ASC 29th Technical Conference, September 8-10, 2014, La Jolla, California.

17. National Aeronautics and Space Administration. 2014. "EFT-1 MSA Fracture Control Plan," EFT1-SPIO-PLAN-00C4, Revision B, March 4, 2014.

18. National Aeronautics and Space Administration. 2008. "Fracture Control Requirements for Spaceflight Hardware," NASA Technical Standard, NASA-STD-5019.

19. Whitcomb, J.D., and K.N. Shivakumar. 1989. "Strain-Energy Release Rate Analysis of Plates with Postbuckled Delaminations," *J. Compos.Mater.,* 27(7): 714-734.

20. Nilsson, K., -F., J.C. Thesken, P. Sindelar, A.E. Giannakopoulos, and B. Storåkers. 1993. "A Theoretical and Experimental Investigation of Buckling Induced Delamination Growth," *J. Mesh. Phys. Solids*, 41(4): 749-782.

21. Reeder, J.R., K. Song, P.B. Chunchu, and D.R. Ambur. 2002." Postbuckling and Growth of Delaminations in Composite Plates Subjected to Axial Compression," presented at the 43rd AIAA/ASME/ASCE/AHS/ASC Structures, Structural Dynamics, and Materials Conference, April 22-25, Denver, Colorado.

22. Krueger, R. 2002. "The Virtual Crack Closure Technique: History, Approach and Applications," *NASA/CR—2002-211628*.

23. Kellas, S., B. Lerch., and N. Wilmoth. 2012. "Mechanical Characterization of In- and Out-of-Autoclave Cured Composite Panels for Large Launch Vehicles," presented at SAMPE 2012, May 21-24, 2012, Baltimore, Maryland.

24. Singer, J., J. Arboz, and T. Weller. 1998. *Buckling Experimental Methods in Buckling Thin Walled Structures, Basic Concepts, Columns, Beams and Plates – Volume 1*. John Wiley & Sons, Inc., New York.

25. Ko, W.L. 1987. "Accuracies of Southwell and Force/Stiffness Methods in the Prediction of Buckling Strength on Hypersonic Aircraft Wing Tubular Panels," *NASA/TM-88295*.

26. Jones, R.E., and B.E. Greene. 1976. "Force/Stiffness Technique for Nondestructive Buckling Testing," *J. Aircraft*, 13(4):262-269.

27. Abaqus. 2013. *Abaqus Analysis User's Guide (Abaqus Online Documentation), version 6.13*. Dassault Systèmes Simulia Corp., Providence.

28. National Aeronautics and Space Administration. 2008. "Structural Design and Test Factors of Safety for Spaceflight Hardware," NASA Technical Standard, NASA-STD-5001A.

29. National Aeronautics and Space Administration. 1968. "Buckling of Thin-Walled Circular Cylinders," NASA SP-8007, 1968.

30. Ortiz, M. and A. Pandolfi. 1999. "Finite-Deformation Irreversible Cohesive Elements for Three-dimensional Crack-Propagation Analysis," *Int. J. Numer. Meth. Engng.*, 44: 1267-1282.

31. Xie, D. and A.M. Waas. 2006. "Discrete Cohesive Zone Model for Mixed-Mode Fracture Using Finite Elements," *Eng. Frac. Mech.*, 73: 1783-1796.

32. Jones, R.M. 1999. *Mechanics of Composite Materials, 2nd Edition,* Taylor & Francis, Inc.